Biophysical Journal

Supporting Material

Quantitative Analysis and Modeling Probe Polarity Establishment in C. elegans Embryos

Simon Blanchoud, Coralie Busso, Félix Naef, and Pierre Gönczy

Supporting Material

Image analysis

PAR-2 levels were determined between late prophase (centration/rotation) and metaphase either on fixed specimen by immunofluorescence or on live embryos expressing GFP::PAR-2 (Fig. S1 E-F). Two regions of interest per embryo (posterior membrane *PM* and posterior background *PB*) were manually defined using a circular selection tool 9 pixels in diameter (Fig. S1 D) with the ImageJ software (1) and their pixel intensity analyzed with Matlab 2012b. Camera white noise and its standard deviation σ were automatically estimated (2) and averaged for each genotype. Posterior cortical signal was defined in a signal-to-noise ratio approach as $(PM - PB) / \sigma$ to compensate for the out-of-focus illumination visible in the posterior cytoplasm and normalized by setting the average of the wild-type measurements to 100% and the average of the *par-2(RNAi)* to 0%.

All recordings were automatically segmented and analyzed by ASSET (3) and the quantifications implemented either in Matlab 2012b or in C (all code used in this work is available upon request). To capture precisely the signal from the cortex, we developed a model of the image that consists of the background (both from the cytoplasm and the camera), the autofluorescence of the eggshell and the signal *per se* (Fig. S1 H-M). We approximated the cortical signal with a succession of 2D Gaussian functions $I = Ae^{-\frac{(x-\mu)^2}{2\sigma}}$, where A is the amplitude of the signal, μ the position of its center and σ its width. Spatial correlation between the values of the parameters of the model was imposed; in particular, we consider a constant thickness of the membrane by imposing σ to be constant throughout a recording. The background was taken as the smoothed projected image from which the cortex was deleted by replacing the portion between $\mu - 5\sigma$ and $\mu + 5\sigma$ with a linear interpolation of pixel intensity values at the border of this domain. The remaining parameters of the signal were then determined using a Levenberg-Marquardt optimization procedure developed by Manolis Lourakis. The autofluorescence of the eggshell is estimated from the GFP::PAR-2 channel on portions of the eggshell far enough from the cortex ($> 3\sigma$) using the same model as for the cortical signal, but constrained to a single set of parameters for each frame, and subtracted from

the cortical signal as a Gaussian function of the distance between the cortex and the eggshell. The different kymographs utilized to compute the temperature averages (Fig. 2 A and 5 A-C) were aligned such as to minimize their residuals.

We compensated for posteriorization, i.e. the process that re-centers the growing posterior domain to the closest pole (4, 5), by segmenting the center of the GFP::PAR-2 expression kymographs using dynamic programming (DP, 6), minimizing a cost function that mirrored the characteristics of the posterior domain. This function posited that the posterior domain is symmetric, relatively bright, centered at the posterior pole during maintenance and devoid of invaginations. Similarly, the position of the front of the posterior domain was determined using DP with a scoring function that favored pixels on the edge of a bright domain whose intensity value resembles the one observed during the maintenance phase. The parameters used in the different scoring functions were manually optimized through visual inspection and incorporated into a configuration file for ASSET. The duration of polarity maintenance was defined as the time between the moment the front of the domain, as identified by the automatic segmentation, has reached 77.5 % of its final length and the end of the recording (i.e. cytokinesis onset). This percentage was chosen as it corresponds to the portion of lowest variability (as defined by the mean of the squared residuals), taking steps of 2.5 %, when comparing the segmentation of the kymographs aligned for averaging. Note that this percentage also outperforms alignments based on the manual registration of cell cycle events (pronuclear meeting, pseudo-cleavage or cytokinesis onset).

Mathematical modeling and simulations

The model M1 (Eq. 2-3, 7) consists of a one-dimensional (assuming rotational symmetry along the longitudinal axis of the embryo) two-species (modeling the anterior and the posterior complexes at the plasma membrane) partial differential equation (as the model depends both on time and space). The model is composed of the following mathematical terms (Eq. 2):

(i) Rate of change in the concentration of the complexes at the plasma membrane.

(ii) Diffusion: the complex can freely diffuse when bound to the plasma membrane.

(iii) Mutual inhibition: one complex is excluded from the plasma membrane by the other complex. Each inhibition term contains a cooperativity factor (i.e. the exponents α and β) representing the degree of cooperative binding one complex exhibits when excluding the other complex from the membrane. Importantly, if either α or β is greater than one, the system can exhibit local bistability, which is necessary to achieve both a stable uniform unpolarized state at the onset of the process and a stable polarized state during the maintenance stage (7).

(iv) Binding: the complex binds from the cytoplasmic pool (Eq. 2) to the membrane.

(v) Unbinding: the complex detaches from the membrane to the cytoplasmic pool at a given rate.

(vi) Cortical flows: the complexes are displaced toward the anterior pole through an advection process. The resulting depletion of anterior complexes A near the posterior pole is the perturbation that permits the complex P to access the membrane to initiate polarity establishment. Note that cortical flows v vary over space and time.

This model assumes a constant total amount of proteins and a homogeneous cytoplasm; thus, the cytoplasmic pool is the difference between the membrane bound and the total amount of proteins (Eq. 3, 7), where ρ_A and ρ_P are the total amount of A and P respectively, L is the length of the cell membrane and φ is the surface to volume ratio relating the cortical and the cytoplasmic pools. φ is defined for a 3D ellipsoid with semiaxes $a \geq b \geq c$ as the ratio between the surface area S (Eq. 4, 8), where $F(\phi,k)$, $E(\phi,k)$ are incomplete elliptic integrals of the first and second kind respectively, $cos(\phi) = c/a$, and the ellipsoid volume is $V = \frac{3}{4}\pi abc$. Note that the semi-axis c is inferred from b using the result of a linear regression on the data extracted from differential interference contrast (DIC) 3D stacks of twenty embryos with a z resolution of 0.5 µm. The result of the regression is $c = 18.81 - 0.31b$ (R^2=0.99). The assumption that the cytoplasmic pool is well mixed is supported by the fast diffusion rates measured in the cytoplasm and the absence of cytoplasmic GFP gradient (9). Goehring and co-workers have experimentally determined the diffusion constants D_A and D_P, the on binding rates k_{A+} and k_{P+}, the off binding rates k_{A-} and k_{P-}, as well as the relative concentrations ρ_A and ρ_P (7, 9). We

utilized the geometric properties of each cell in the experimental dataset to define the surface to volume ratio φ as well as the membrane length L in the mathematical model in conjunction with the published parameter values (Table S1) and our flow measurements (Fig. 2 C).

All simulations of the model were performed using custom software developed in C, using finite-differences methods to solve the partial differential equations (PDE). For the spatial discretization, the diffusion is solved using a five-point central difference approximation, the advection using a second-order upwind scheme and the integral using the trapezoidal rule. Null derivative (Neumann) boundary condition was used for the protein concentration. The temporal discretization uses a Runge-Kutta-Fehlberg algorithm implemented by John Burkardt. While the time stepping is adaptive, simulations were carried out with 256 meshpoints, thus resulting in a spatial resolution of □0.25 μm, depending on the proportions of the simulated embryo. The initial concentrations used for the simulations were taken as the numerically identified value of the fixed point, in the absence of diffusion and advection, corresponding to the anterior complex being enriched at the membrane (7).

Model optimization

To quantitatively compare the results of the simulation of the mathematical model (Eq. 2-3, 7) with the data acquired in this work, the kymographs need to be synchronized to relate experimentally determined timing of one embryo with that of others, as well as to the timing of a simulation. To do so, we introduced for each embryo a shift factor δ_I for a given simulation S with respect to the experimental kymograph I, which is optimized together with the other parameters of the model. In addition, every kymograph is rescaled by setting the 0.1 % of the outer pixels, as defined by the segmentation of the posterior domain, to zero, and the 99.9 % of the inner pixels to one. Finally, to permit a meaningful comparison between the simulation and the experimental data, we adapted the spatial size of the simulation, L and φ, to match the dimensions of each embryo. We measure the length of the plasma membrane in the midplane of the embryo using the segmentation produced by ASSET to set L and we calibrate the surface to volume ratio of the embryo φ accordingly.

To quantify the resemblance between experiments and simulations, we defined the negative log-likelihood of a parameter set θ, given the set of experimental data Ω (Eq. 1), where I is a M_I by N_I pixels kymograph, S the corresponding simulated kymograph, D and B the positions of the domain boundary for I and S, respectively. The difference in pixel value (i.e. the right term) is rescaled by ε/N_I to have a weight comparable to that of the difference in boundary position (i.e. the left term) in the final score, given that typically $N_I \gg M_I$, where ε is a factor used to balance the influence of the pixel intensity with respect to the position of the boundary that was set to 0.25. In addition, a sigmoid function is applied to the boundary term to prevent the likelihood from being too sensitive to very minor changes in the segmentation of the posterior boundary. The boundary position term was added to the likelihood function to compensate for the lower sensitivity during the initiation stage (e.g. Fig. S2 E), which is due to a lower pixel intensity value at that time compared to the maintenance stage.

The optimization procedure was carried out in alternation by an evolution strategy with covariance matrix adaptation (CMA-ES, 10) and a Nelder-Mead simplex method (fminsearch, 11), both implemented in Matlab. Initial parameter values were generated by adding Gaussian noise first to the published values (7), then to the best values identified, finally to the average of the best value per embryo (Fig. 3). The best value among all these independent optimization runs was utilized in this work. In the optimization of the temperature adaptation models (Fig. S11), the four unmeasured parameters as well as the required shift factors δ_I were optimized together with the parameters of the various models.

Because our experimental setup does not provide information on the dynamics of the anterior domain, whereas the optimization procedure infers parameter values for this domain, we performed a set of 80 simulation experiments to assess the precision of such inferences (Fig. S7). In each experiment, a kymograph is simulated with the published values (7) for the four unmeasured parameters of the model (i.e. k_{AP}, α, k_{PA} and β), Gaussian white noise is added and the optimization procedure utilized to find back these values. Half of the optimization procedures were initialized at the correct values (k_{AP} = 0.19, α = 1, k_{PA} = 2 and β = 2), the other half further away from these values, at position where polarity could still be established (k_{AP} = 0.026, α = 1.97, k_{PA} = 0.014 and β = 2.42).

In addition, as described above, the shift factor δ_I was optimized as a fifth parameter, with the value of 0 being utilized for the simulated kymograph. Finally, different amounts of noise (10%, 25%, 50% and 100% of the parameter value) were added to the initial parameter value to study the convergence of the optimization procedure. With the exception of four optimizations that did not converge properly (i.e. that were detected as outliers based on their log-likelihood score using the algorithm detailed in the next paragraph), all 76 remaining simulation experiments converged properly towards the parameter value used in the simulation (Fig. S7). Importantly, the precision of the optimization procedure is maximal for the two cooperativity exponents α and β (Fig. S7 H, K).

To identify sets of parameters as outliers (i.e. $\{k_{AP}, \alpha, k_{PA}, \beta, \mathcal{L}\}$ in Fig. 3), we followed a principal component based approach that has been designed for multi-dimensional data (12). Given the amount of noise present in our data, we increased empirically the tolerance of this detection method, utilizing a larger c parameter by taking 25 times the median absolute deviation (MAD) of the distance, instead of 2.5, in the first biweight function (i.e. w_{1i}). We utilized the same algorithm for outliers identification in the convergence analysis (Fig. S7) but multiplying the MAD by 5.

Estimating cortical flows

To obtain a spatial and temporal map of the dynamics of cortical flows, we followed an indirect approach that utilizes the displacement of sub-cortical cytoplasmic yolk granules as a proxy for the movements of the contracting cortex. Importantly, while GFP::NMY-2 foci are best observed using cortical imaging (13), VIT-2::GFP permits midplane imaging, and thus the monitoring of movements both close to the male pronucleus during the early onset of flows as well as at the poles after posteriorization. Because measuring cortical flows obviously requires localizing the cortex, we inferred the position of the cell membrane in these frames (Fig. S4 A) using DP with a cost function based on VIT-2::GFP intensity. To infer the center of the forthcoming posterior domain, we detected the position of the male pronucleus by identifying the areas devoid of granules using two different intensity thresholds (Fig. S4 B), fitting the largest inscribed circle in each of these areas (Fig. S4 C) and tracking them over time until

pronuclear meeting using a custom implementation of a published algorithm (14). All the code utilized for measuring cortical flows was implemented using Matlab 2012b.

We detected the position of the fluorescent VIT-2::GFP granules (Fig. S4 D) by utilizing the "à trous" wavelet transform (Fig. S4 E, 19) to obtain an initial estimate, combined with an approach developed for super-resolution microscopy (16) to refine our detection (Fig. S4 F). A custom merging algorithm then discarded faint spots and computed the weighted average of overlapping particles (Fig. S4 G). The detected spots were then used as initial estimates for a second iteration of our detection pipeline (Fig. S4 H). The granules were then tracked using a custom implementation of an algorithm that performs this task by global optimization of the set of particle trajectories (Fig. S4 I, 18) without the gap closing, merging and splitting steps that were too computationally intensive for being implemented in this context. All the short tracks (< 5 frames) were then discarded; the directed speed of each remaining granule was then computed.

To determine the speed of the cortical flow at a particular location along the plasma membrane, we utilized a weighted average of the directed speeds using a spatial Gaussian kernel to favor exponentially more granules closest to the cortical actomyosin network. Such an approach should provide a more robust quantification than considering merely the closest granules. To quantify the precision of this approach, as well as to identify the most suitable kernel size, we carried out a set of simulation experiments using published velocity distributions of VIT-2::GFP granules (Fig. S5 A, (17)). We fitted cubic smoothing splines (csaps in Matlab) on the published values for the average posterior speed of the granules, as well as on the corresponding standard deviation, to infer a smooth speed distribution over the 14 µm range measured experimentally by those authors. This permits us to simulate sets of velocities for a given number of granules and with a distribution matching that of the experimental data, thus comparing the precision of different approaches for inferring the cortical speed (Fig. S5 B). We computed the error of the estimated cortical speed over 5000 realizations (i.e. the absolute difference with the true value), as well as its standard deviation, for a number of kernel sizes and particle number (Fig. S5 C, D). As anticipated, Gaussian weighting outperforms standard average for a wide range of kernel sizes, in particular for lower number of granules (Fig. S5 C). Interestingly, while larger kernels provide the less variable estimates (Fig. S5 D),

their inferred value is less precise on average because they take into account lower speeds further away from the cortex, hence underestimating the actual value at the cortex (Fig. S5 C). In the context of this trade-off between robustness and precision, we define the most adequate kernel size as the one minimizing the average error plus standard deviation between 10 and 450 granules (with a step size of 20 granules). Optimization was carried out using an evolution strategy with covariance matrix adaptation (CMA-ES, 10) and the best identified value found to be 0.895 µm (Fig. S5 E). Finally, to identify a potential bias in the inferred cortical speed, we computed the average estimated speed over the aforementioned range of granule number, and found it to be 92.8 % of the true value (Fig. S5 F). We thus compensate all cortical flow measurements for the 7.2 % underestimate inherent to a kernel of size 0.895 µm

A running average with a temporal window of 10 frames was applied to reduce the noise in the estimated velocities. The component of the velocity parallel to the segmentation of the cortex was kept (17). Finally, we compensated for posteriorization by performing this analysis relative to the position of the male pronucleus, which we tracked using the same algorithm (14). We quantified the cortical flows in recordings acquired in six embryos, tracking the movements of 1'729'820 particles in total, and aligned the embryos temporally to minimize the sum of flow map residuals. Note that because of the assumed rotational symmetry of polarity establishment, the two sides of the embryo were combined and thus flows are perfectly symmetric (Fig. 2 C). These 2D flows were utilized in all simulations except the original models (M1 and M1*), for which the original 2D flows were utilized (7). The flow values provided in Tables S1 and S2 were computed by averaging the pixels brighter than the mean plus two standard deviation of the respective 2D flow profiles.

In addition, we repeated this quantification by substituting the particle tracking step by particle image velocimetry (PIV, Fig. S6). PIV is a widespread flow quantification technique that has been used notably to quantify cortical flows in *C. elegans* (7, 17). Here, we utilized an ImageJ plugin to perform iterative PIV analysis (18). This comparison confirmed that the quantified flow profiles agreed between the two methods, both for individual recordings (Fig. S6 A-C), for the average flow profiles (Fig.

2 C and S6 D) and for the measured cortical speeds (Table S2), although a lower spatial resolution was obtained using PIV.

Cortical flows dependence on cell size

Assuming that the strength of the cortical flows depends on the fraction of bound myosin motors on actin filaments (19), it follows that these forces should depend on the inverse of the surface to volume ratio φ. For simplicity, we define the binding of myosin (M) on actin filaments (F) as a reversible three steps process (Eq. 5), where M_c and M_m are the fractions of cytoplasmic and membrane-bound myosin motors respectively, F_c and F_m the fraction of cytoplasmic and membrane-bound actin filaments and FM the force generating complex. We then write the law of mass action corresponding to the defined concentrations (Eq. 6) with symmetric equations for F_c and F_m. In addition, we hypothesize that the total pools of both myosin motors and actin filaments are fixed (Eq. 7), where M_T and F_T are the two total concentrations and φ is the surface to volume ratio. Moreover, because we want to determine the relation between FM and the proportions of the cell, we assume steady state for all the reactions. Finally, for simplicity, we approximate the cortical concentration of actin F_m as being constant (assuming the concentration of myosin motors is limiting, $k_B F_m = k_{BF}$); however, the relation between FM and φ computed without this hypothesis leads to the similar conclusion. Under these hypotheses, one can then compute the relation between FM and M_T.

Temperature dependence models

To adapt the model to variations in temperature, we considered three different equations for the diffusion constants (D^i, D^{ii}, D^{iii}), three for the biochemical reaction rates (k^i, k^{ii}, k^{iii}) and three for the flows (v^i, v^{ji}, v^{jii}). For all three mechanisms, the model i assumes a constant value for all the temperatures, thus being supposedly the worst model, and is used for comparison with more elaborate models. On the contrary, all models iii utilize independent values for each temperature. Note that, with the exception of k_{AP}, k_{PA} and v, which were not measured experimentally at 20 °C (9), all other parameters of the model have the published value (Tables S1, S2) imposed at 20 °C (i.e. all the temperature dependence models equal one at this temperature).

For the dependence to temperature of the reaction rates and flows, we utilized the Arrhenius equation $k_T = ke^{-\frac{E_k}{k_B T}}$, where k represents the so-called prefactor, E_k the activation energy of the reaction, T the absolute temperature in Kelvin and k_B the Boltzmann constant. This approach has been applied to a wide variety of biological processes, ranging from isolated biochemical reactions (20) to entire organisms (21). For the flows, we hypothesized that these are proportional to the fraction of active motors bound to actin filaments while the force of each motor remains constant (19), hence converting them to a motor binding reaction rate. For the adaptation of the diffusion coefficients to changes in temperature, we utilized the Stokes-Einstein equation $D_T = \frac{k_B T}{\zeta \eta_T}$, where η_T is the viscosity of the fluid and ζ the drag coefficient of the diffusing particle. Importantly, η_T itself depends on temperature through an unknown function. However, we approximate this relation using a thermally activated Arrhenius equation $\eta_T = \eta e^{\frac{E_D}{k_B T}}$, which is valid for colloidal gels (22).

Because the experimental measurements of the different reactions rates were performed at 20 °C on average (9), we set out to compute the conversion factors f_{kT} and f_{DT} that define the value of the different parameters at a temperature T such that $k_T = f_{k_T} k_{20}, D_T = f_{D_T} D_{20}$. We thus obtained two equations (Eq. 8-9) that depend only on the temperature T, their respective activation energy E_k and E_D as well as the Boltzmann constant k_B. In addition, we also optimized scaling parameters for k_{AP}, k_{PA} and ν because their value was not measured experimentally at 20 °C. All parameter values are provided in Table S4.

Equations

$$(1)\quad -\log \mathcal{L}(\theta \mid \Omega) = \sum_{I \in \Omega} \frac{M_I}{2} \log\left(\sum_{i=1}^{M_I} \frac{1}{1+e^{-(B_{i+\delta_I} - D_i)^2}} + \frac{\varepsilon}{N_I} \sum_{i=1}^{M_I} \sum_{j=1}^{N_I} \left(S_{i+\delta_I, j} - I_{i,j} \right)^2 \right)$$

$$\frac{\partial A}{\partial t} = D_A \frac{\partial^2 A}{\partial x^2} - k_{AP} A P^{\alpha} + k_{A_+} A_c - k_{A_-} A - \frac{\partial (\nu A)}{\partial x} \Bigg| \text{anterior complex}$$

(2)

$$\underbrace{\frac{\partial P}{\partial t}}_{\text{i}} = \underbrace{D_P \frac{\partial^2 P}{\partial x^2}}_{\text{ii}} - \underbrace{k_{PA} P A^{\beta}}_{\text{iii}} + \underbrace{k_{P_+} P_c}_{\text{iv}} - \underbrace{k_{P_-} P}_{\text{v}} - \underbrace{\frac{\partial (\nu P)}{\partial x}}_{\text{vi}} \Bigg| \text{posterior complex}$$

(3)

$$A_c = \rho_A - \frac{\varphi}{L} \int_{-\frac{L}{2}}^{\frac{L}{2}} A \mathrm{d}x$$

$$P_c = \rho_P - \frac{\varphi}{L} \int_{-\frac{L}{2}}^{\frac{L}{2}} P \mathrm{d}x$$

(4) $$S = 2\pi c^2 + \frac{2\pi ab}{\sin(\phi)} \left(E(\phi, k) \sin(\phi)^2 + F(\phi, k) \cos(\phi)^2 \right)$$

$$F_c \underset{k_{F-}}{\overset{k_{F+}}{\rightleftharpoons}} F_m$$

(5) $$M_c \underset{k_{M-}}{\overset{k_{M+}}{\rightleftharpoons}} M_m$$

$$F_m + M_m \underset{k_D}{\overset{k_B}{\rightleftharpoons}} FM$$

$$\frac{dM_c}{dt} = k_{M-} M_m - k_{M+} M_c$$

(6) $$\frac{dM_m}{dt} = k_{M+} M_c - k_{M-} M_m - k_B F_m M_m + k_D FM$$

$$\frac{dFM}{dt} = k_B F_m M_m - k_D FM$$

(7)

$$F_T = F_c + \varphi F_m + \varphi FM$$

$$M_T = M_c + \varphi M_m + \varphi FM$$

$$(8)\ f_{k_T} = \frac{k_T}{k_{20}} = \frac{ke^{-\frac{E_k}{k_B T}}}{ke^{-\frac{E_k}{k_B T_{20}}}} = e^{-\frac{E_k}{k_B}\left(\frac{1}{T}-\frac{1}{T_{20}}\right)}$$

$$(9)\ f_{D_T} = \frac{D_T}{D_{20}} = \frac{\frac{k_B T}{\zeta \eta_T}}{\frac{k_B T_{20}}{\zeta \eta_{20}}} = \frac{T}{T_{20}}\frac{\eta_{20}}{\eta_T} = \frac{T}{T_{20}} e^{-\frac{E_D}{k_B}\left(\frac{1}{T}-\frac{1}{T_{20}}\right)}$$

Supporting Tables

- **Table S1.** Published parameters of the model (Eq. 2-3). All the values are taken from published results (7, 9). Parameters determined empirically are highlighted with a gray background. v was computed by averaging the pixels brighter than the mean plus two standard deviation of the published 2D flow profile. φ and L were computed assuming a 54×30×30 µm embryo.

		Meaning	*Value*	*Std*	*Units*
Anterior domain	D_A	Diffusion coefficient	0.28	0.05	µm^2/s
	k_{AP}	Inhibition rate	0.19	-	µm^2/s
	α	Cooperativity exponent	1	-	-
	k_{A+}	Binding rate	0.00858	0.0017	µm/s
	k_{A-}	Unbinding rate	0.0054	0.005	1/s
	ρ_A	Total protein concentration	1.56	0.33	1/µm^3
Posterior domain	D_P	Diffusion coefficient	0.15	0.03	µm^2/s
	k_{PA}	Inhibition rate	2	-	µm^4/s
	β	Cooperativity exponent	2	-	-
	k_{P+}	Binding rate	0.0474	0.012	µm/s
	k_{P-}	Unbinding rate	0.0073	0.0057	1/s
	ρ_P	Total protein concentration	1	-	1/µm^3
	v	Cortical flows	0.1 [a)]	0.015 [a)]	µm/s
	φ	Surface to volume ratio	0.174	-	1/µm

L	Membrane length	134.6	-	µm

- **Table S2**. Published cortical flow speeds. Note that *N* corresponds to the number of particle tracked in the first two references, while it corresponds to the number of embryo analyzed in the other references. [a)] The value was computed by averaging the pixels brighter than the mean plus two standard deviation of the corresponding 2D flow profile. [b)] The value was computed by integrating the portion of the smoothed curve (as described in SM: Estimating cortical flows) above the mean plus one standard deviation of the corresponding 1D flow profile.

Reference	*Speed (µm/s)*	*N*	*Technique*
(23)	0.067 ± 0.013	17	Manual tracking of microinjected fluorescein-phalloidin aggregates
(24)	0.067 ± 0.008	≥48	Slope of DIC granules kymograph
This work	0.071 ± 0.008 [a)]	6	VIT-2::GFP particle tracking
This work	0.075 ± 0.011 [a)]	6	VIT-2::GFP particle image velocimetry
(17)	0.080 ± 0.007 [b)]	6	VIT-2::GFP particle image velocimetry
(25)	0.090 ± 0.007 [b)]	75	NMY-2::GFP particle image velocimetry
(7)	0.11 ± 0.015 [a)]	4	NMY-2::GFP particle image velocimetry
(13)	0.128 ± 0.017	6	Slope of NMY-2::GFP kymograph

- **Table S3.** Calibrated values for the unmeasured parameters. The two first models utilize the published empirical values (7). Note that lower values for the mutual inhibition rates (k_{AP} and k_{PA}) are required to account for the low GFP::PAR-2 signal on the anterior half of the embryo (Fig. S2). Units are as in Table 1.

	k_{AP}	α	k_{PA}	β
M1 (7)	0.19	1	2	2
M1* (optimized values)	0.001	4.81	0.075	3.15
M2 (new flows)	0.19	1	2	2
Average of all best values	0.043 ± 0.12	1.97 ± 1.26	0.34 ± 1.39	2.14 ± 0.78

Average without outliers	0.008 ± 0.017	2.17 ± 1.28	0.030 ± 0.035	2.30 ± 0.74
M3 (size calibrated)	0.002	2.09	0.014	2.36
M4 (temperature model)	0.002 ± 0.001	2.09 ± 0.16	0.014 ± 0.001	2.36 ± 0.09

- **Table S4**. Parameters of the various temperature models (Fig. S11, see Materials and Methods). Note that for the models *iii*, the two values correspond to the direct impact of temperature on the rates at 13 °C and 24 °C respectively (i.e. instead of an activation energy as written in the header). Note also that v represents the scaling applied to the cortical flows (Fig. 2 C) at 20 °C. Units are as in Table S1.

Fig. S11	*Model*	k_{AP}	k_{PA}	v	E_D	E_k	E_v
A	D^{ii}, k^{ii}, v^{j}	0.0027	0.0144	0.81	0.85	0.32	0
B	D^{i}, k^{i}, v^{j}	0.0028	0.0146	0.79	0	0	0
C	D^{ii}, k^{ii}, v^{ji}	0.0025	0.0136	0.87	0.88	0.36	0.0001
D	$D^{iii}, k^{iii}, v^{iii}$	0.0025	0.0138	0.87	1.34;1.69	1.02;1.20	1.08;0.75
E	D^{i}, k^{ii}, v^{j}	0.0025	0.0135	0.79	0	0.0001	0
F	D^{i}, k^{i}, v^{ji}	0.0026	0.0140	0.78	0	0	0.0007
G	D^{i}, k^{ii}, v^{ji}	0.0025	0.0136	0.76	0	0.0014	0.0014
H	D^{ii}, k^{i}, v^{j}	0.0025	0.0137	0.90	0.32	0	0
I	D^{iii}, k^{i}, v^{j}	0.0026	0.0142	0.84	0.85;1.36	0	0
J	D^{iii}, k^{ii}, v^{ji}	0.0025	0.0136	0.75	0.48;1.53	0.36	0.0003
M4	D^{ii}, k^{ii}, v^{j}	0.0023	0.0132	0.86	0.80	0.23	0

Supporting Movie

- **Movie S1**. Representative triple channel time-lapse recording of a wild type GFP::PAR-2; *par-2(ok1723)*; mCherry::PH embryo. The recorded channels are (top) DIC, (middle) mCherry::PH, (bottom) GFP::PAR-2; the raw data is displayed in each case. This recording corresponds to the frames used in Fig. 1 and S1 and has been accelerated 60 times. See also Fig. S1D.

Supporting Figures

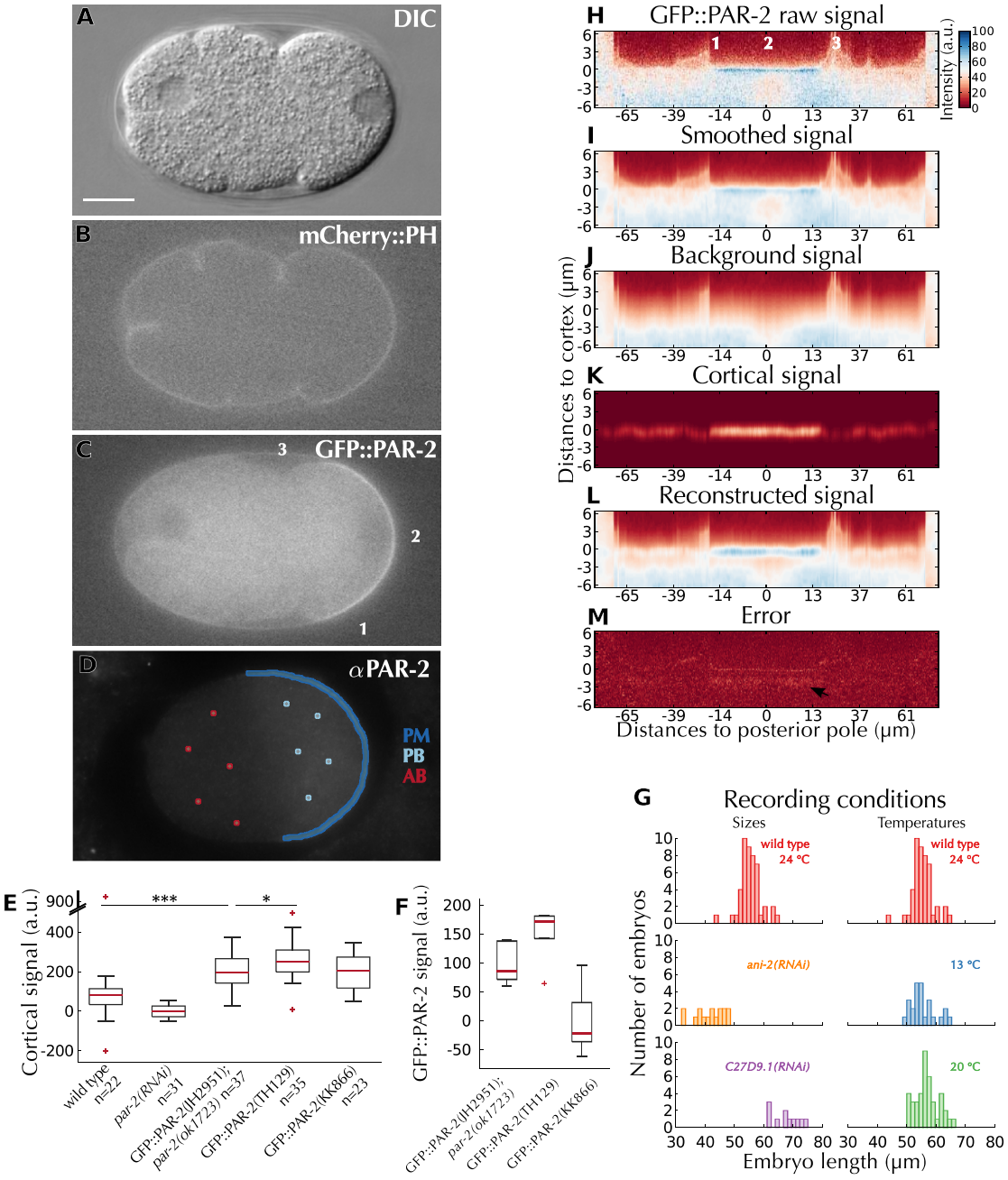

- **Figure S1**. Monitoring polarity establishment. (**A-C**) Frame from representative triple channel time-lapse recording (**A** DIC, **B** mCherry::PH, **C** GFP::PAR-2). Numbers in **C** and **H** denote corresponding locations. Scale bar: 10 µm. (**D**) Sample immunofluorescence image from the strain used in this study, overlaid with the two manually defined regions of interest (color-coded) utilized for signal quantification (see

Supporting Material). *AB* represents what we considered as the anterior background, by opposition to the quantified posterior background (*PB*). (**E**) Comparison of PAR-2 protein levels in strains of indicated genotype. The means of the RNAi and of the wild type are defined as 0% and 100%, respectively. The strain used in this study is JH2951, the one used by Goehring *et al.* TH129. For each boxplot, the horizontal red line represents the median, the box ranges from the 25th to the 75th percentile and the whiskers extend to the entire distribution of data points with the exception of outliers depicted by red crosses. Note that in all figures, statistical significance (here using a Student's two-tailed *t*-test) is indicated by: * $p < 0.05$, ** $p < 0.01$, *** $p < 0.001$. (**F**) Comparison of the expression level of the GFP::PAR-2 transgene in strains of indicated genotype. *n=5* for every genotype. (**G**) Distribution of embryo lengths in different recording conditions: *ani-2(RNAi)* (*n=16*), *C27D9.1(RNAi)* (*n=11*), 24 °C (*n=47*), 13 °C (*n=25*), 20 °C (*n=41*). The 24 °C is represented twice for comparison with both datasets. (**H**) Raw perpendicular quantification of the image in **C** based on the segmentation performed by ASSET. (**I**) Perpendicular quantification of image in **C** smoothed using a Gaussian filter. The background signal (**J**) is separated from the cortical signal (**K**) as described in the Supporting Material. (**L**) Signal reconstructed using the described quantification procedure. (**M**) Difference between **H** and **L** indicate that only little information is lost below the posterior domain (arrow).

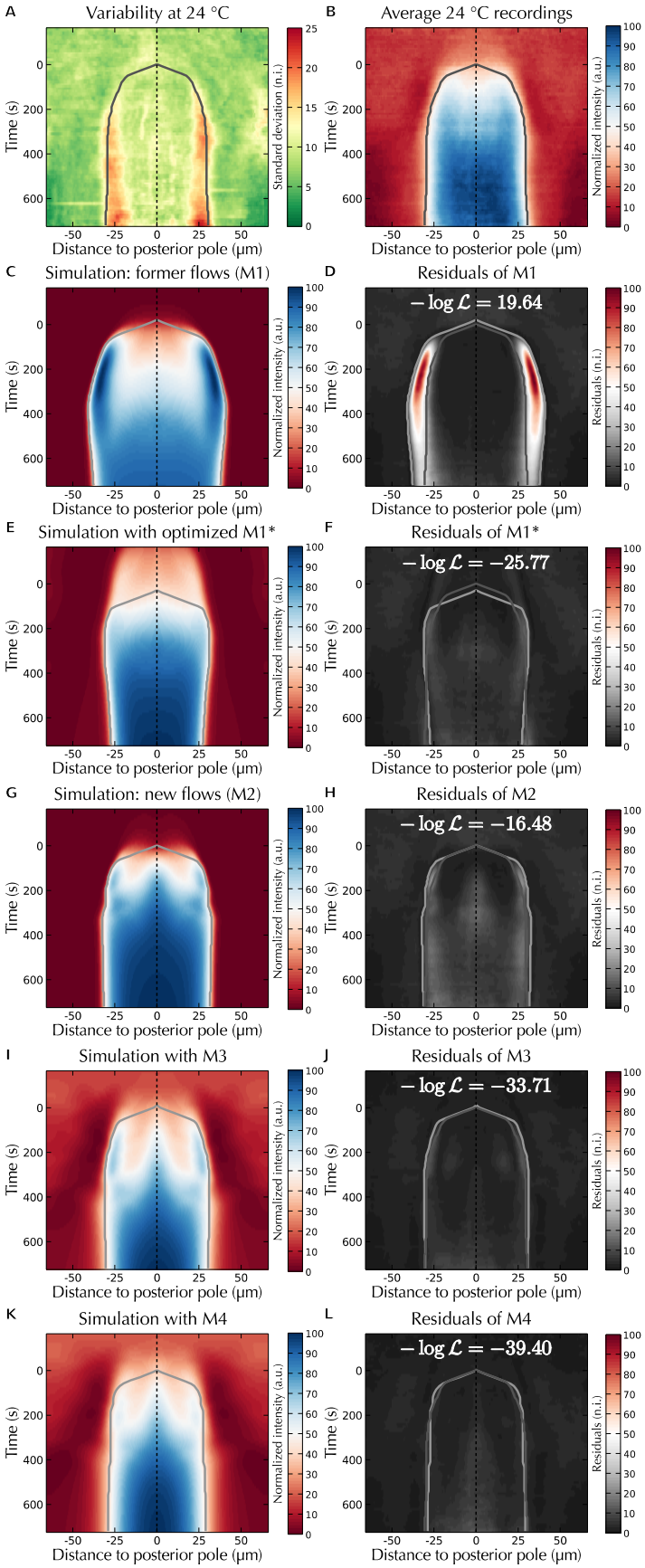
A
Variability at 24 °C
B
Average 24 °C recordings
C
Simulation: former flows (M1)
D
Residuals of M1
$-\log \mathcal{L} = 19.64$
E
Simulation with optimized M1*
F
Residuals of M1*
$-\log \mathcal{L} = -25.77$
G
Simulation: new flows (M2)
H
Residuals of M2
$-\log \mathcal{L} = -16.48$
I
Simulation with M3
J
Residuals of M3
$-\log \mathcal{L} = -33.71$
K
Simulation with M4
L
Residuals of M4
$-\log \mathcal{L} = -39.40$
Time (s)
Distance to posterior pole (µm)
Standard deviation (n.i.)
Normalized intensity (a.u.)
Residuals (n.i.)

- **Figure S2**. Prediction of the model with new cortical flow measurements is quantitatively improved with respect to experimental data. (**A**) Standard deviation of the average corresponding to **B** (n.i.: normalized intensity, i.e. the same scale as **B**). Note that the highest variation is located along the boundary of the domain towards the end of polarity maintenance. (**B**) Average protein expression during polarity establishment at 24 °C, overlaid with segmentation of the center of the domain (dashed black line) and of the domain expansion (dark gray). (**C**) Simulation of the mathematical model from Goehring *et al.* (Eq. 2-3) using the published parameter values and cortical flows (Table S1). The kymograph is overlaid with the segmentation of the domain (light gray). (**D**) Residuals between the experimental data in **B** and the simulation in **C**, overlaid with both segmentations and the negative log-likelihood score. (**E**) Same as in **C** but using optimized parameter values. (**F**) Residuals between the simulation in **B** and the experimental data in **E**, overlaid with both segmentations, using the same color map as **D**. (**G-H**) Same as in **C-D** but as predicted using the flows quantified using VIT-2::GFP particle tracking. The absence of leading edge enrichment is reflected in the reduction of the log-likelihood. (**I-J**) Same as in **C-D** but as predicted using model M3 (i.e. after calibration with the median kymographs). (**K-L**) Same as in **C-D** but for model M4 (i.e. implementing in addition the most likely temperature dependence model calibrated on the median kymographs, Fig. 6).

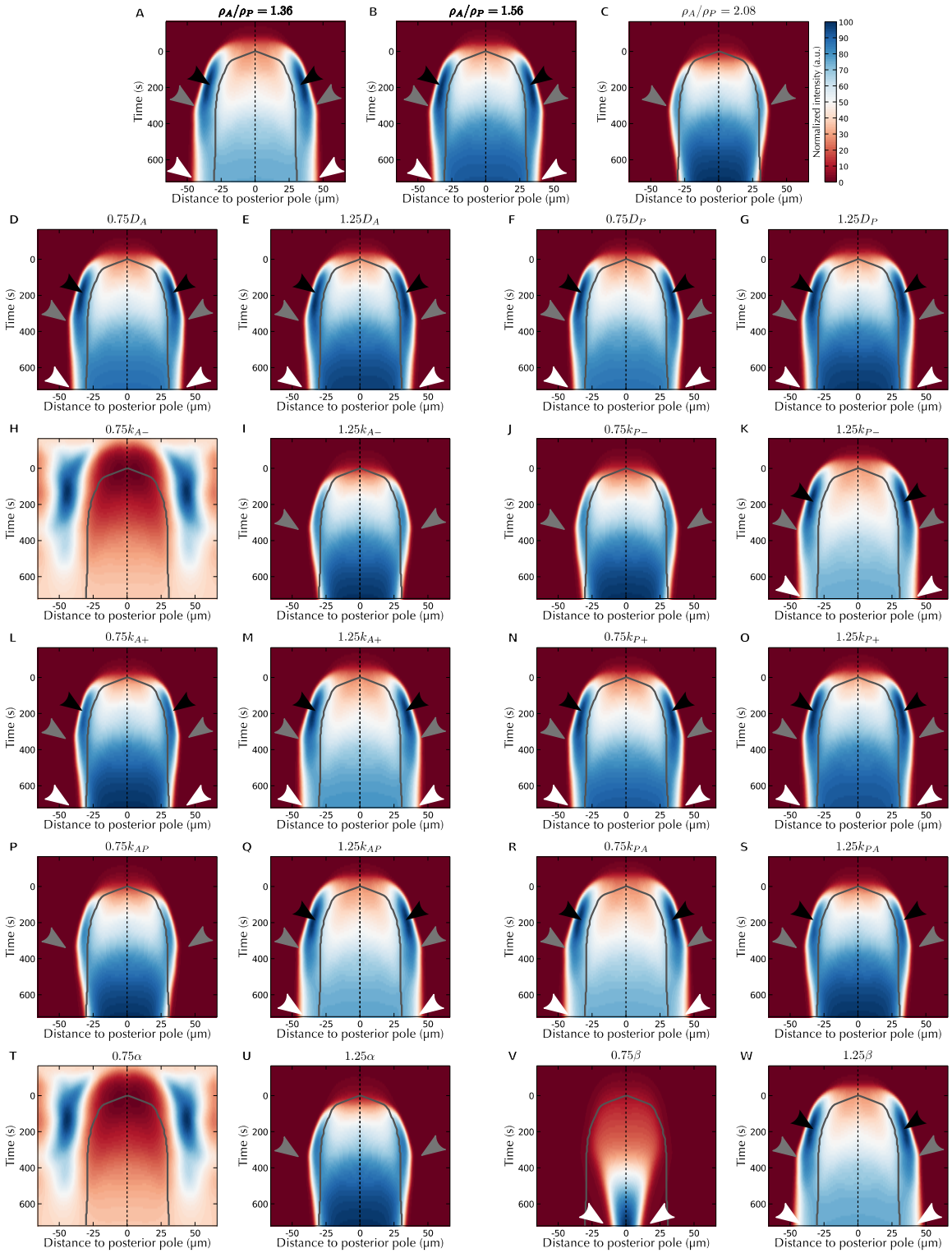

- **Figure S3**. Varying published parameter values does not attenuate leading edge enrichment. (**A-C**) Varying the relative level of posterior proteins. Simulation of the mathematical model from (7) using the published parameter values and cortical flows

(M1) with the indicated relative level of posterior proteins (above). The kymograph is overlaid with the segmentation of the experimental domain at 24 °C (dark gray) and the center of the domain (dashed black line). The relative concentration of the anterior versus posterior proteins (ρ_A/ρ_P) has been measured experimentally, using the ratio between the fluorescence expression of GFP::PAR-6 and GFP::PAR-2, to be 1.56 (i.e. **B**, (7)). Black arrowheads indicate the salient leading front enrichment not observed experimentally (see Fig. 2 A), gray arrowheads the concomitant domain overshooting and white arrowheads point at the extent of the posterior domain. (**D-E**) Same as **A** and **C** but varying the anterior diffusion coefficient D_A. Note that the reference kymograph for this variation is still **B**. (**F-G**) Same as **D-E** but varying the posterior diffusion coefficient D_P. (**H-K**) Same as **D-G** but varying the binding rates k_{A+} and k_{P+}. (**L-O**) Varying the unbinding rates k_{A-} and k_{P-}. (**P-S**) Varying the mutual inhibition rates k_{AP} and k_{PA}. (**T-W**) Varying the cooperativity coefficients α and β. Note that in **H** and **T**, polarity is not established because of the high uniform level of the posterior proteins throughout the simulation. Note also that none of these variations corrects both the enrichment and the overshooting.

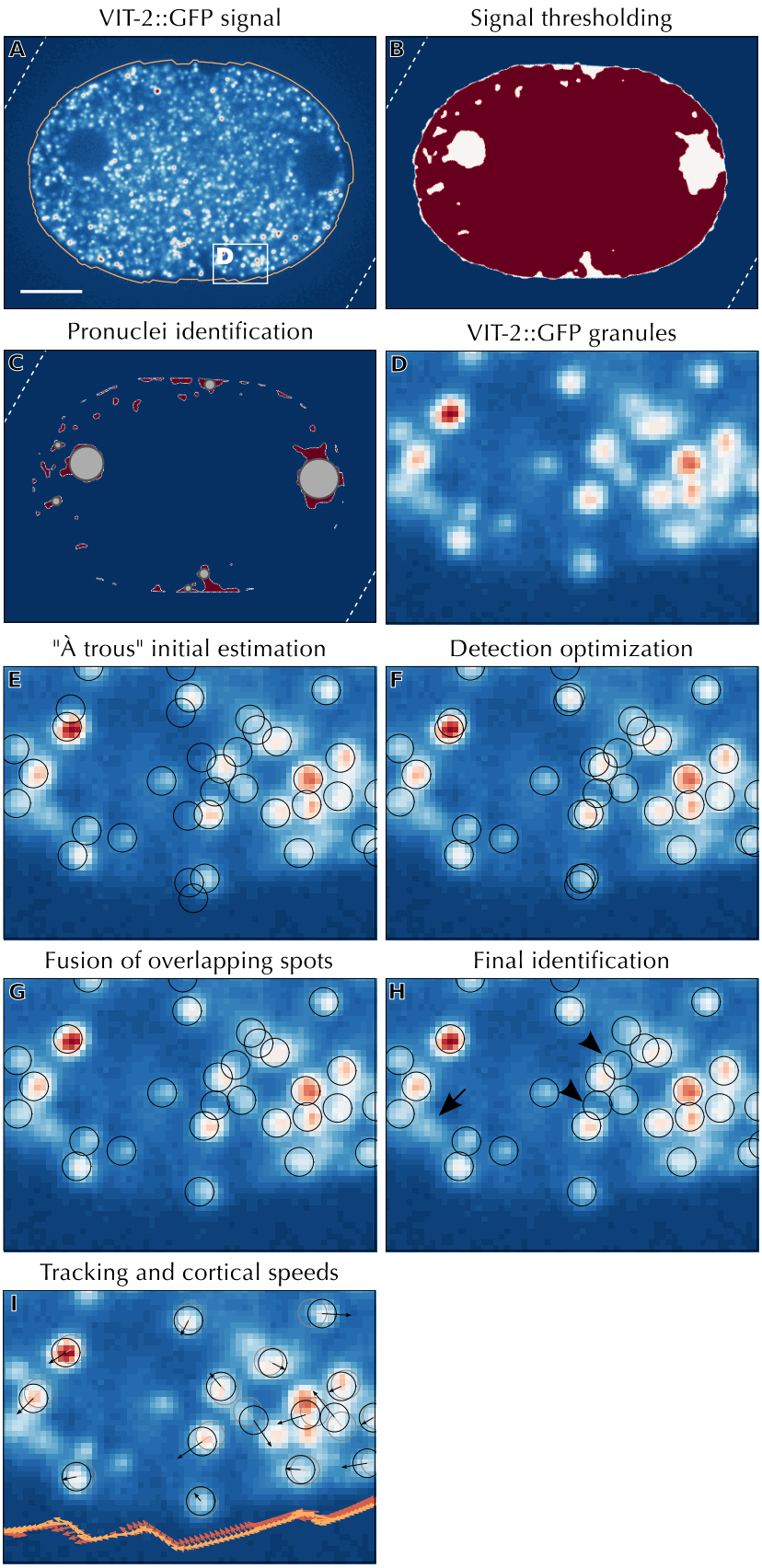
VIT-2::GFP signal
Signal thresholding
A
B
D
Pronuclei identification
VIT-2::GFP granules
C
D
"À trous" initial estimation
Detection optimization
E
F
Fusion of overlapping spots
Final identification
G
H
Tracking and cortical speeds
I

- **Figure S4**. Detection and tracking of VIT-2::GFP granules. (**A**) Raw GFP image utilized to detect the yolk granules overlaid with the segmented cortex (orange). The scale bar represents 10 µm and the white box delimits the area magnified in panels **D-I**. The white dashed lines in **A-C** delimit the boundary of the raw image. (**B**) Segmentation of the GFP image using two different intensity thresholds. The lower one delimits the entire embryo (white) while the higher one retains the area in which granules can be located (red). (**C**) Identification of candidate positions for the pronuclei. The areas devoid of granules (red) are overlaid with the largest inscribed circles (gray) representing candidate pronuclei. (**D**) Magnification of the area delimited in **A**. (**E**) Localization using the "à trous" wavelet transform. (**F**) Result of the spot detection optimization procedure (see Supporting Material). (**G**) Fusion of the overlapping detections in **F**. (**H**) Final estimation after a second round of optimization and fusion. The arrow indicates a missed granule, the arrowheads detection mistakes, typically discarded by the tracking algorithm (see Supporting Material). (**I**) Tracking of the detected yolk granules (black circle) linked with their position in the previous frame (gray circle) and the resulting displacement (black arrow). The averaged displacement (red) and the component parallel to the cell cortex (i.e. cortical flow, orange) are depicted on the cell membrane.

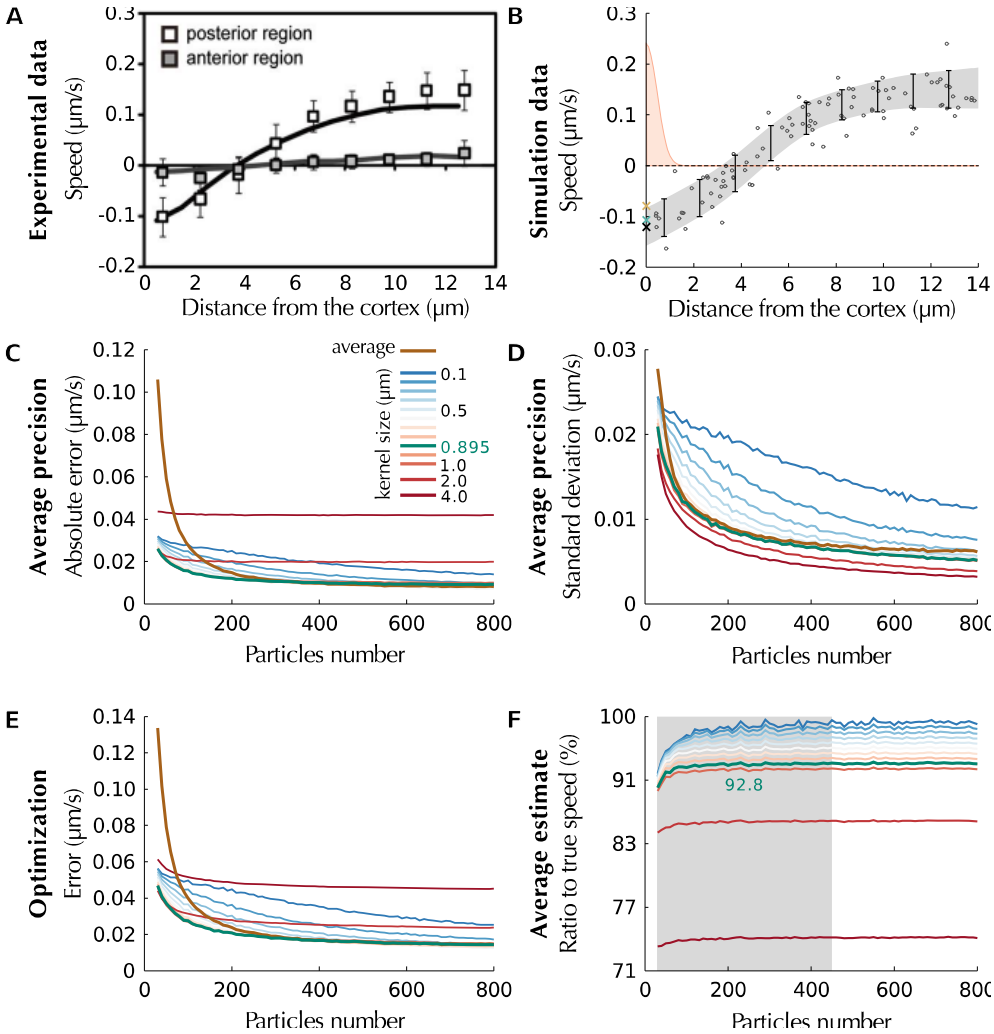

- **Figure S5.** Precision of cortical flow measurements using particle tracking. (**A**) Published *in vivo* speed distribution of VIT-2::GFP granules (from 17). (**B**) Simulation experiment of 100 granule speeds following the distribution in **A** (black circles). Overlaid are the averages and standard deviations extracted from **A** (black), their polynomial interpolation (gray), the extrapolated cortical speed (black cross), the weight distribution for the optimal Gaussian kernel size of 0.895 µm (pink, see SM), the corresponding cortical speed estimation (turquoise cross) and the estimation obtained by averaging the 15 closest granules from the cortex (brown cross). (**C**) Comparison of the average precision of the estimated cortical flow for a wide range of granule number and kernel sizes, color-coded as indicated. (**D**) Standard deviation of the corresponding estimates in **C**, color-coded as in **B**. (**E**) Error function used by the optimization algorithm to identify

the most adequate kernel size (average plus standard deviation), color-coded as in **B**. (**F**) Average estimated cortical speed for the kernel sizes color-coded as in **B**. Overlaid in gray is the range of granule numbers, the average of which was used to compensate the underestimation resulting from a kernel size of 0.895 µm.

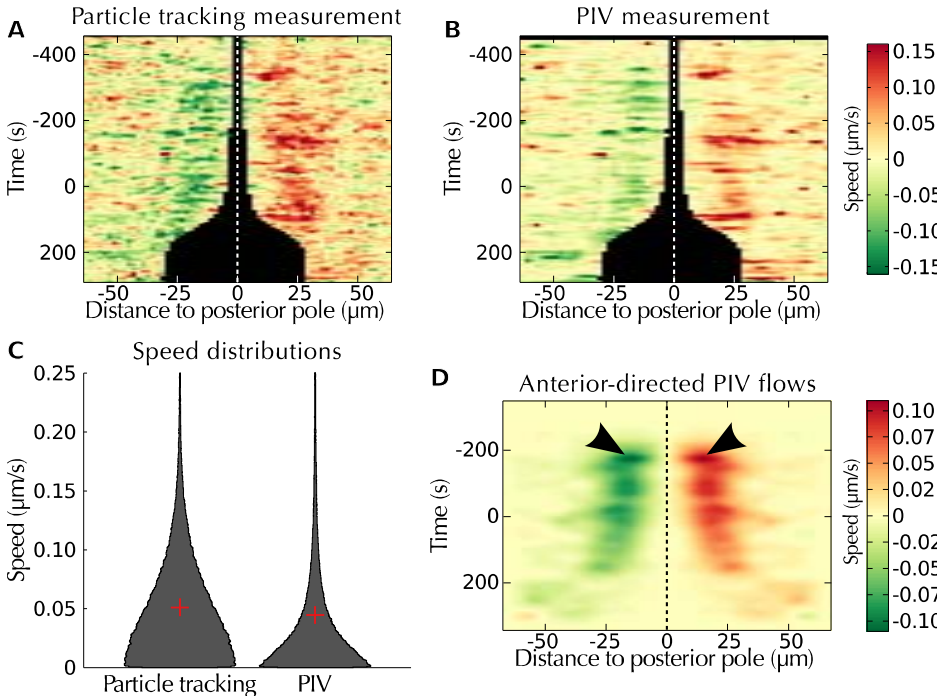

- **Figure S6.** Cortical flow quantification using particle image velocimetry (PIV). (**A**) The cortical flow profile of a single VIT-2::GFP recording using the particle tracking approach (see Fig. S4 and S5). The black area in the center of the flow profile corresponds to the portion of the cortex masked by the male pronucleus. (**B**) The cortical flow profile of the same recording as in **A** but using PIV instead of particle tracking. The color code is identical between **A** and **B**. Note that except for the lower resolution obtained in **B**, the two profiles appear almost identical. (**C**) Comparison of the distribution of speed magnitudes between the particle tracking approach and PIV. All six flow profiles were pooled for these violin plots where the normalized histogram of speed magnitudes is depicted in black and the corresponding mean value as a red cross. Note that mean value for PIV (0.045 µm/s) is slightly lower than for particle tracking (0.051 µm/s). Note also that a long tail in both distributions was cut at 0.25 µm/s. (**D**) The average 2D flow profile obtained using PIV. Note that, except for a stronger initial pulse (arrowheads), the PIV approach leads to similar results than the presented particle tracking method (compare with Fig. 2 C).

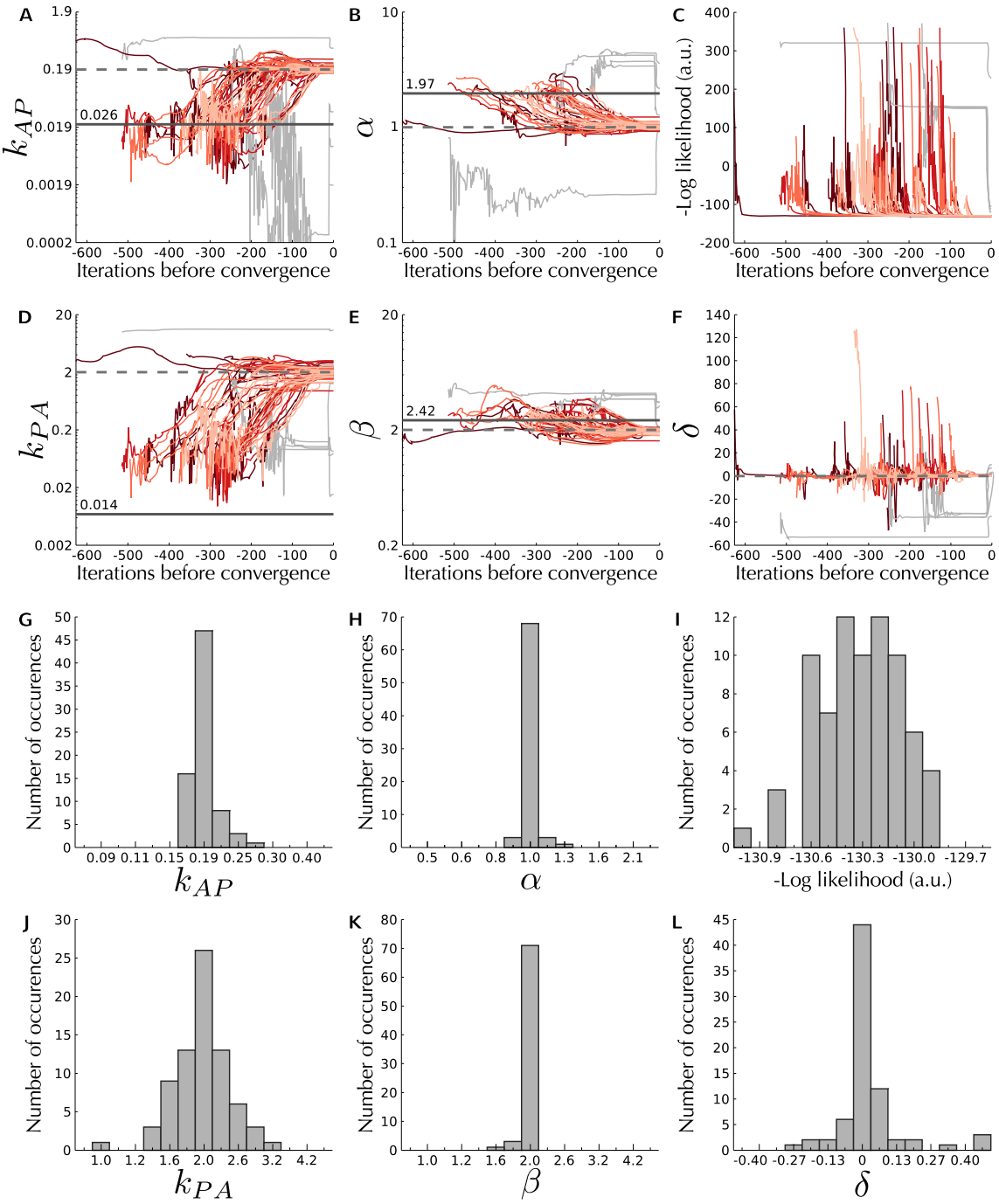

- **Figure S7**. The maximum-likelihood optimization procedure converges in simulation experiments. (**A-F**) Time traces for the optimization procedure of the indicated model parameters in 80 simulations experiments. Half of the optimization procedures were initialized around the correct values (depicted by the dashed gray line) while the other half were initialized around the values represented by the solid black line, with the corresponding value inscribed above it. Different shades of red indicate different amounts

of noise (10%-lightest, 25%, 50% and 100%-darkest) added to the initial value of the parameters while the gray lines indicate the four optimizations that did not converge properly (i.e. that were detected as being outliers based on their log-likelihood score). Note that no shift was introduced in the reference kymographs, hence the optimal value for the shift factor δ (see SM) is 0. (**G-L**) Distribution of the identified most-likely parameter value after convergence. All four unmeasured parameters, as well as the shift factor δ (see SM), are correctly identified by the optimization procedure. Note that the cooperativity exponents α and β are more tightly defined than the two inhibition rates k_{AP} and k_{PA}. Note also that these simulation experiments were performed using uncompensated cortical flows (i.e. 92.8 % of the actual speeds, see SM: Estimating cortical flows). However, because the convergence of these simulation experiments depends on the smoothness of the parameter space rather than on the cortical flow value, using such reduced speeds does not affect these results.

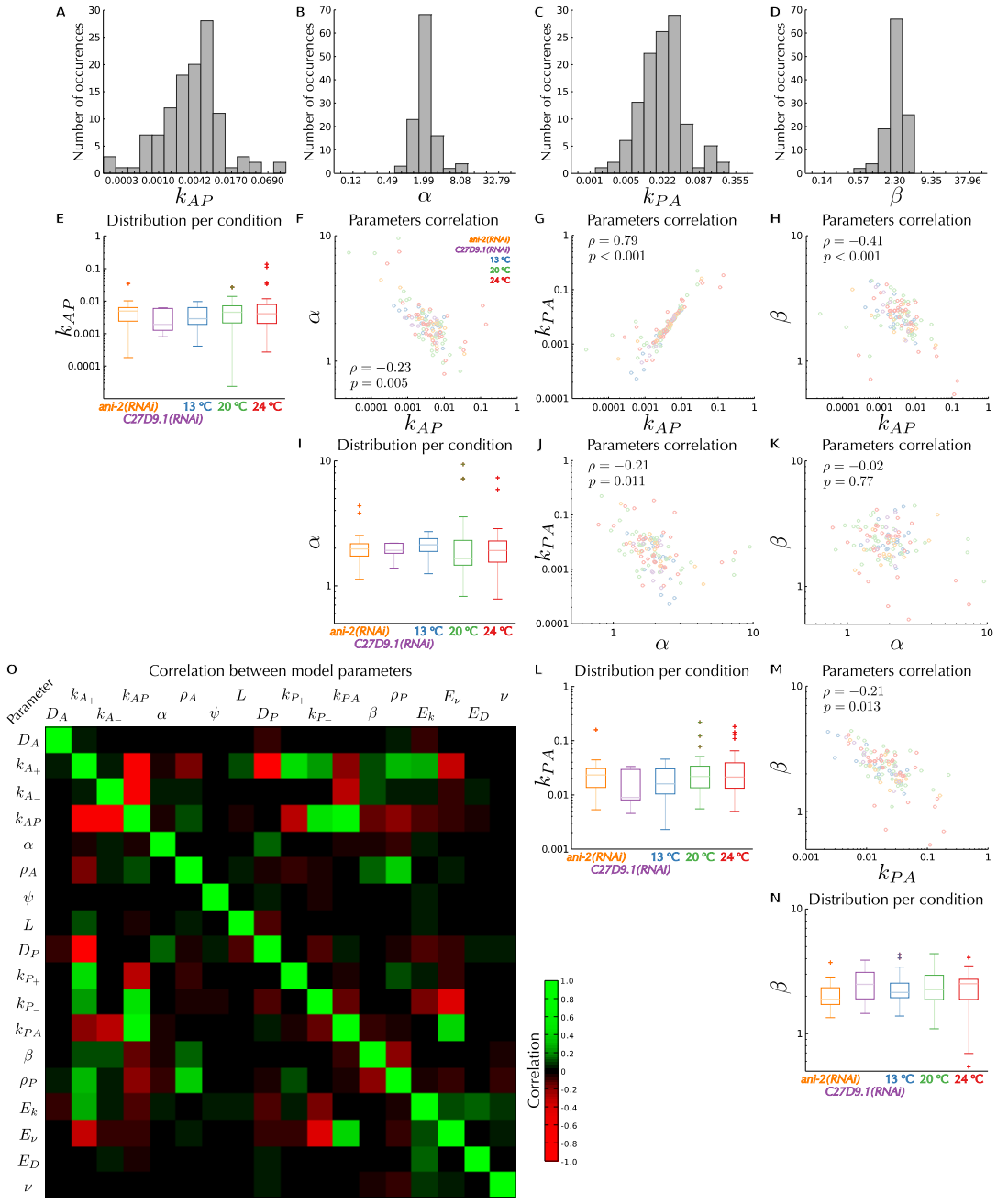

- **Figure S8**. Distribution of the most likely parameters for each embryo. (**A-D**) Distribution of the best value for the unmeasured inhibition parameters identified for each embryo independently. (**E**) Distribution of the inhibition rate k_{AP} per condition, color-coded as indicated. Statistical significance between all five different recording conditions was tested using Student's two-tailed *t*-test. Correlation between k_{AP} and (**F**) the anterior cooperativity exponent α, indicated is the corresponding Pearson's correlation coefficient ρ and the corresponding *p*-value (Student's t-distribution for a transformation of the

correlation), (**G**) the posterior inhibition term k_{PA} and (**H**) the posterior cooperativity term β respectively. (**I**) Distribution per condition of α. Correlation between α and (**J**) k_{PA} and (**K**) β respectively. (**L**) Distribution per condition of k_{PA} and (**M**) its correlation with β. (**N**) Distribution per condition of β. Note the high positive correlation between k_{AP} and k_{PA}, indicating that the value of these two parameters needs to be carefully balanced for polarity to establish properly. Note also the lower correlation observed between the inhibition rates k_{AP} and k_{PA}, and the cooperativity exponents α and β. This implies that a potential underestimation of the inhibition rates would lead to a reduction of the cooperativity exponents. Consequently, maximum care was taken in quantifying the signal on the anterior domain (see SM: Image Analysis) to ensure that k_{AP} or k_{PA} bear their proper values. Note also that, as in the simulation experiments (Fig. S7), the cooperativity exponents α and β are more tightly defined than the two inhibition rates k_{AP} and k_{PA} (compare **B** and **D** with **A** and **C**). (**O**) Correlation matrix for model M4. Each entry in the matrix represents the correlation, as indicated by the color code, between the corresponding column/row pair of parameters of the model. Positive correlation (green) highlights parameters whose joint variation has a minor influence on the likelihood score. On the contrary, negative correlation (red) points at parameters whose mutual compensation influences little the likelihood score. By contrast, black indicates parameters that cannot compensate for each other. The matrix was computed using a numerical approximation of the Hessian matrix (26).

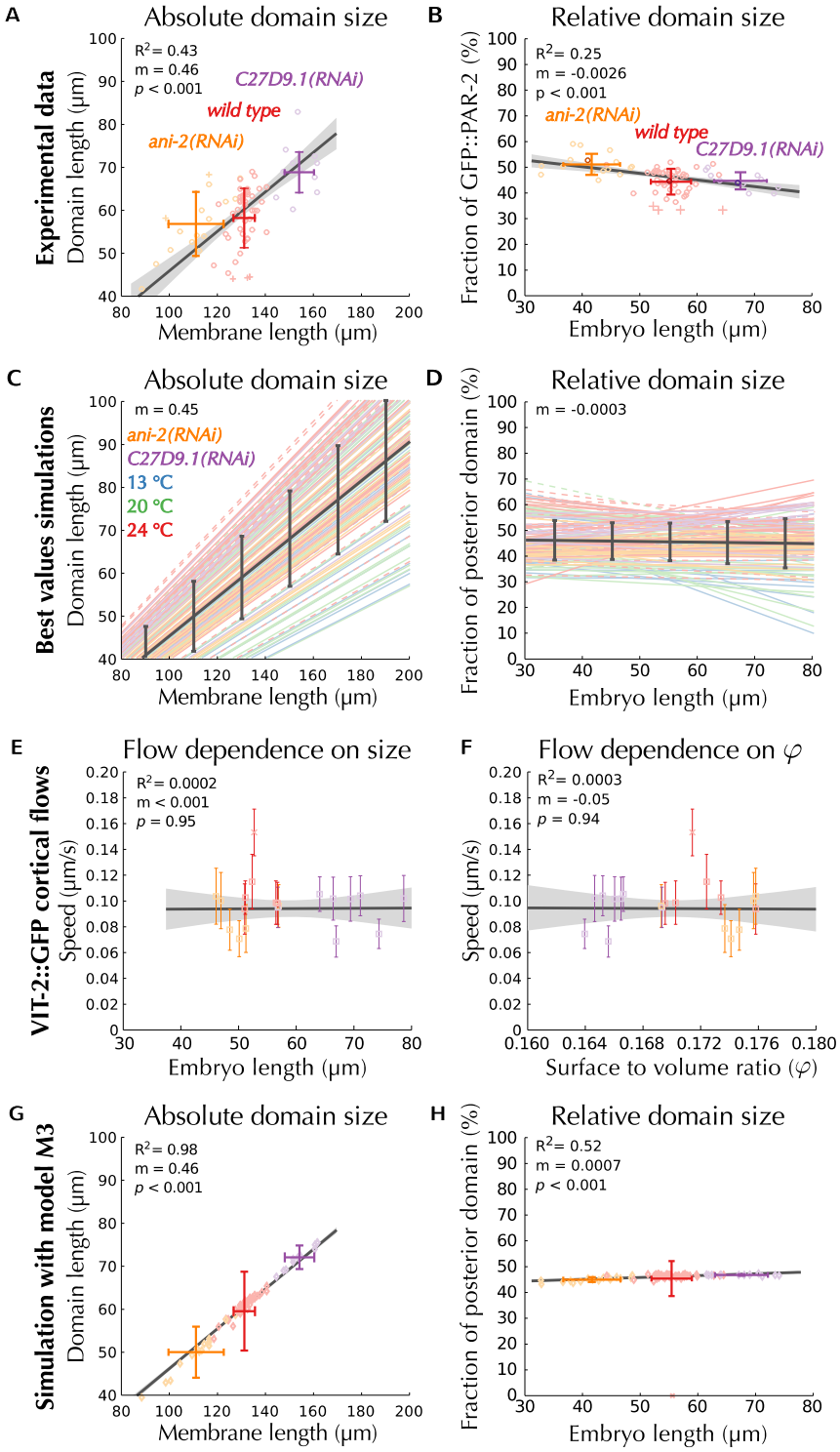

- **Figure S9**. Adaptations of the posterior domain size to variations in embryo size. (**A**) Correlation between membrane length and the length of the posterior domain in embryos from the color-coded recording condition, overlaid with the linear regression (dark gray line), the 95% confidence interval for the estimated regression coefficients (light gray

area), the correlation coefficient R^2, the slope of the correlation m and the p-value (Student's two-tailed t-test for the coefficient m). Note that in this representation of the data, the slope m corresponds to the average length of the posterior domain. (**B**) Correlation between embryo size and the relative fraction of membrane occupied by the posterior domain as observed experimentally, overlaid with the same information as in **A**. The darker circles indicate the location of the median recordings depicted in Fig. 4. Note that **A** and **B** are redundant. However, the imprecision in the domain scaling is more apparent in **B** while **A** is a more intuitive representation of the scaling process. (**C**) Correlation between membrane length and the length of the posterior domain as predicted when the most likely set of parameter values $\{k_{AP}, \alpha, k_{PA}, \beta\}$ of each embryo (see Fig. 3) is utilized. Thin lines represent the linear regression (similar to the thick black line in **A**) obtained from the domain length predicted by a set of parameter value, color-coded as the recording condition the corresponding embryo belongs to (i.e. similar to Fig. 3). Dashed lines correspond to the regression from parameter values identified as outliers in Fig. 3. Overlaid are the average of the regression slopes (black line), the corresponding standard deviation (whiskers) and the slope of the average correlation m. (**D**) Same as C but between embryo size and the relative fraction of membrane occupied by the posterior domain. (**E**) Absence of correlation between embryo length and cortical flow speed. The color code is the same as in **A**. Note that velocities are slightly higher than in Table S2 because here we display the average of the absolute speeds. (**F**) Same as in **E** but between the surface to volume ratio of the embryo and cortical flow speed. (**G**-**H**) Same as in **A** and **B** but as predicted by model M3 (i.e. using the values calibrated with the median recordings). Note also that panels **B** and **H** are the same as Fig. 4 G and H and are depicted here for comparison with **D**.

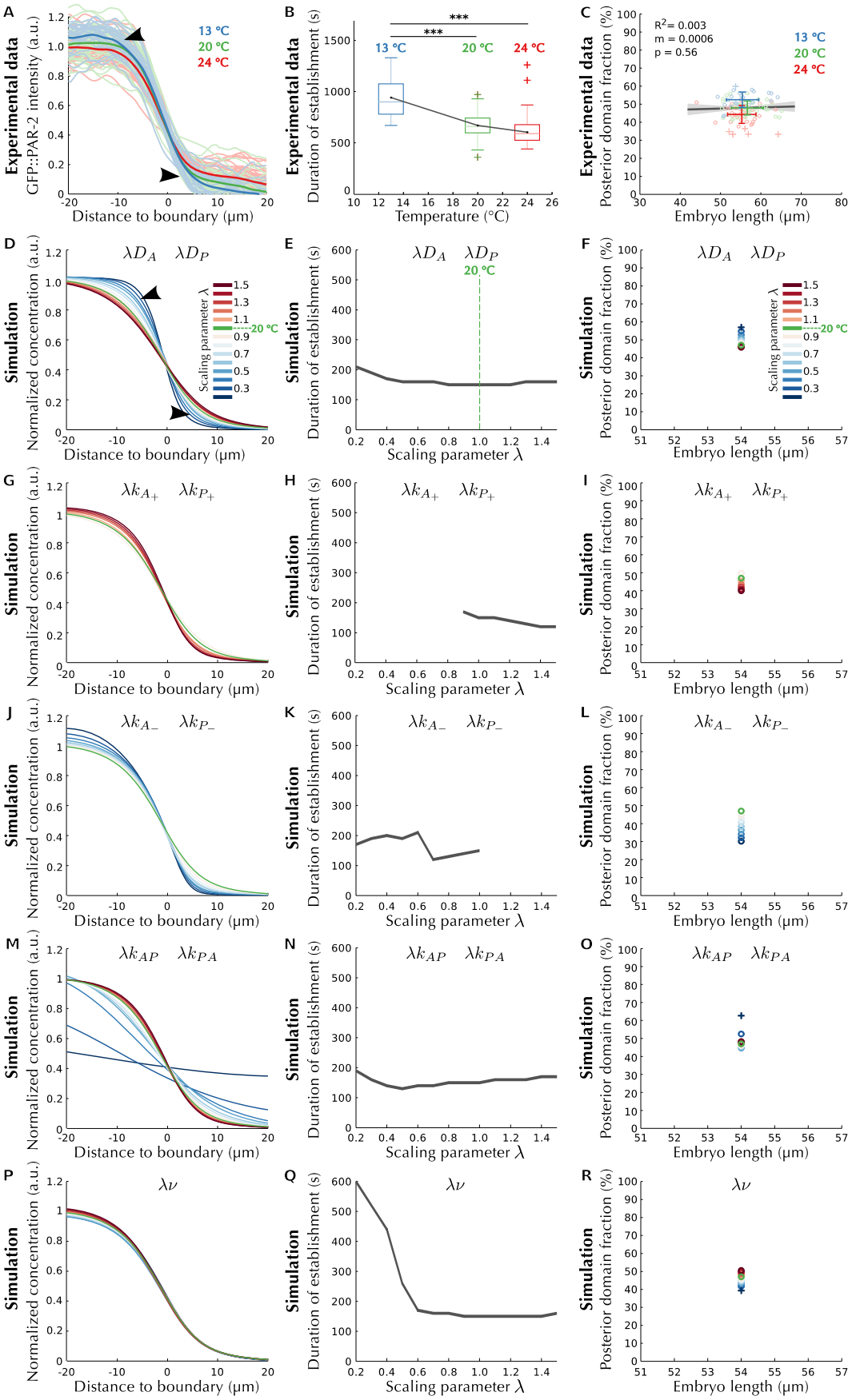
A
Experimental data
GFP::PAR-2 intensity (a.u.)
13 °C
20 °C
24 °C
Distance to boundary (μm)
B
Experimental data
Duration of establishment (s)
***
***
13 °C
20 °C
24 °C
Temperature (°C)
C
Experimental data
Posterior domain fraction (%)
R²= 0.003
m = 0.0006
p = 0.56
13 °C
20 °C
24 °C
Embryo length (μm)
D
Simulation
Normalized concentration (a.u.)
λD_A λD_P
Scaling parameter λ
1.5
1.3
1.1
20 °C
0.9
0.7
0.5
0.3
Distance to boundary (μm)
E
Simulation
Duration of establishment (s)
λD_A λD_P
20 °C
Scaling parameter λ
F
Simulation
Posterior domain fraction (%)
λD_A λD_P
Scaling parameter λ
20 °C
Embryo length (μm)
G
Simulation
Normalized concentration (a.u.)
λk_A+ λk_P+
Distance to boundary (μm)
H
Simulation
Duration of establishment (s)
λk_A+ λk_P+
Scaling parameter λ
I
Simulation
Posterior domain fraction (%)
λk_A+ λk_P+
Embryo length (μm)
J
Simulation
Normalized concentration (a.u.)
λk_A− λk_P−
Distance to boundary (μm)
K
Simulation
Duration of establishment (s)
λk_A− λk_P−
Scaling parameter λ
L
Simulation
Posterior domain fraction (%)
λk_A− λk_P−
Embryo length (μm)
M
Simulation
Normalized concentration (a.u.)
λk_AP λk_PA
Distance to boundary (μm)
N
Simulation
Duration of establishment (s)
λk_AP λk_PA
Scaling parameter λ
O
Simulation
Posterior domain fraction (%)
λk_AP λk_PA
Embryo length (μm)
P
Simulation
Normalized concentration (a.u.)
λν
Distance to boundary (μm)
Q
Simulation
Duration of establishment (s)
λν
Scaling parameter λ
R
Simulation
Posterior domain fraction (%)
λν
Embryo length (μm)

- **Figure S10**. Diffusion is the only process in the model whose variation reproduces the trends observed *in vivo* upon variation of the recording temperature. (**A-C**) Monitoring polarity establishment at three different temperatures (color-coded) exhibits (**A**) a flattening of the domain gradient, (**B**) an increase in the pace of polarization and (**C**) a slight contraction in the relative length of the posterior domain. (**D-F**) Variations in the diffusion coefficients (D_A and D_P jointly) by the nondimensional scaling parameter λ to mimic the impact of temperature in the absence of a temperature dependence model. Upon increasing values of λ (i.e. at increasing temperatures), the model predicts all three trends observed *in vivo*: (**D**) a flattening of the domain gradient (arrowheads), (**E**) an increase in the pace of polarization and (**F**) a slight contraction in the relative length of the posterior domain. Note that because of the absence of a temperature dependence model, the relation between the value of λ and temperature is unknown and thus the y-axis in **D**, the x-axis in **E** and the y-axis in **F** are not directly comparable to those in **A-C**. (**G-I**) Changes in profile, timing and relative domain size when the on rates (k_{A+} and k_{P+}) are varied. (**J-R**) Similar to **D-F** but when the off rates (k_{A-} and k_{P-}), the mutual inhibition rates (k_{AP} and k_{PA}) or the flow speeds (v) are varied, respectively. Note that no other parameter besides the diffusion coefficients (**D-F**) recapitulates all three trends observed experimentally (**A-C**). Note also that some of these rates could potentially be reduced upon increasing temperature. However, no parameter exhibits an inversion in all three trends with increasing λ. In addition, note that panels **A**, **B**, **D** and **E** are the same as Fig. 5 D-G and H and are depicted here for comparison with the other panels.

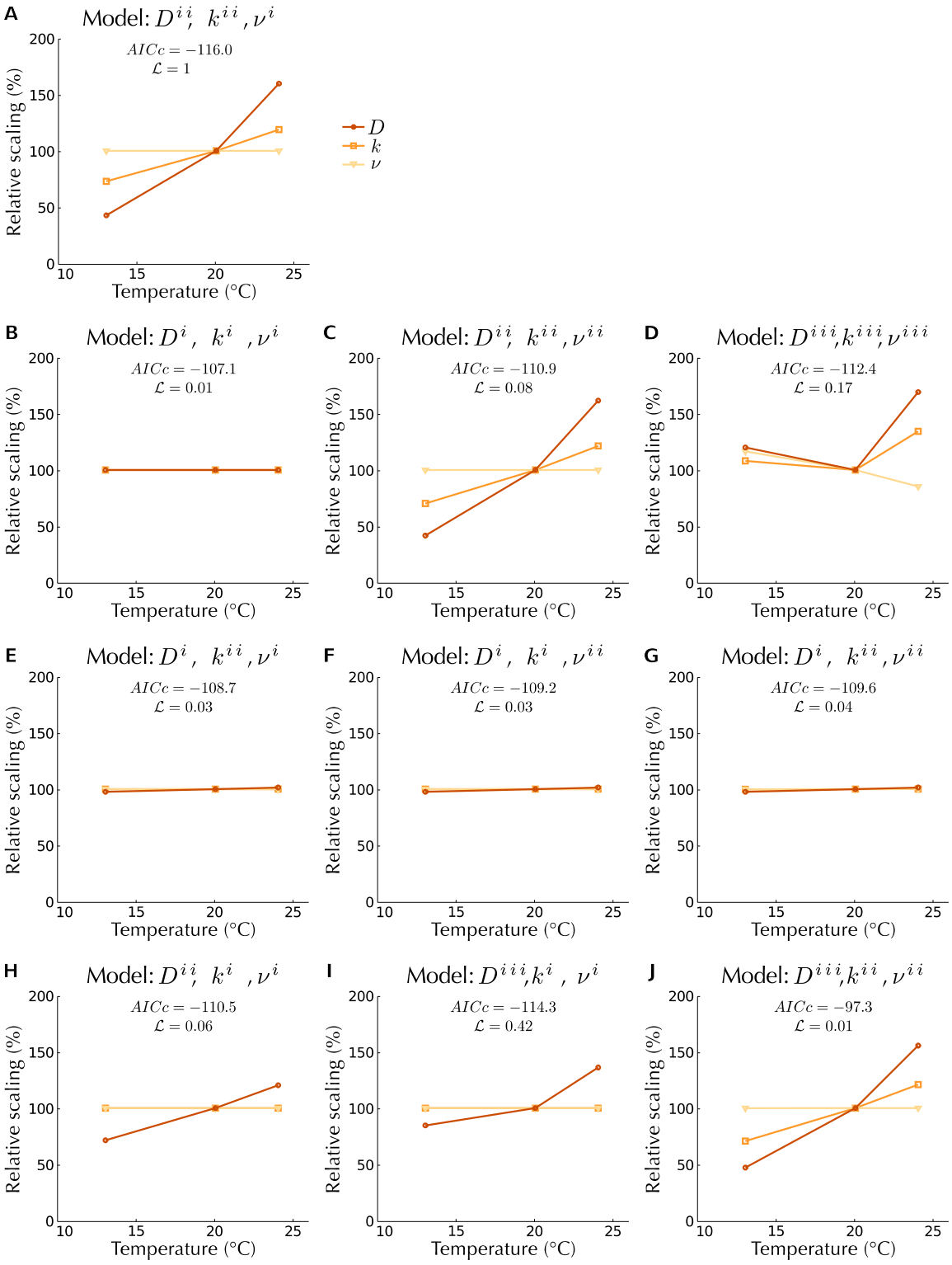

- **Figure S11**. Diffusion and biochemical reaction rates have Arrhenius-like kinetics while flows are temperature invariant. Relative value of the coefficients at the different temperatures, for diffusion (D, circles and dark ochre line), reaction rates (k, squares and

ochre) and cortical flows (ν, triangles and light ochre) for temperature independent models (constant rates, *i*), Arrhenius temperature dependence models (*ii*) or independent values for each temperature (*iii*). Indicated are the performance of each model using the Akaike Information Criterion (AICc) with a correction with the described log-likelihood function (Eq. 1) and the relative likelihood with respect to the highest likelihood model (**A**). All models confirm that diffusion is more sensitive to variations in temperature than biochemical rates (i.e. the dark ochre curve is steeper than the ochre one). In particular, models D^i, in which diffusion is invariant to temperature, restrains the temperature adaptation of both reaction rates and cortical flow (**B, E-G**). Note that in all models, cortical flows are mostly invariant with respect to temperature. In particular, ν^j (**A**) outperforms ν^{ji} (**C**), supporting an apparent compensation mechanism to changes in temperature.

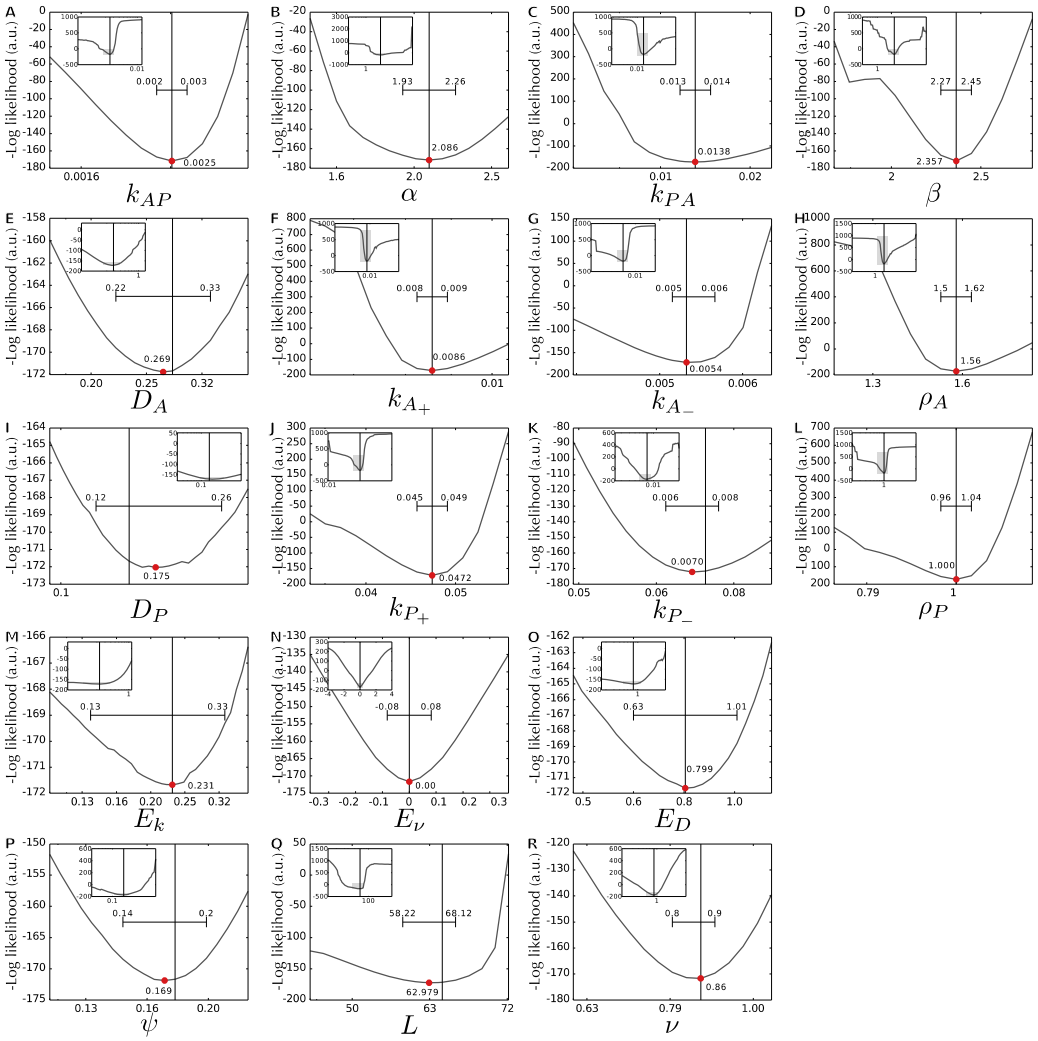

- **Figure S12**. Sensitivity analysis of model M4 with respect to the experimental dataset. This analysis was performed using the model corresponding to Fig. S10 J on the three temperature average kymographs (see Fig. 5 A-C). Each panel displays the value of the negative log-likelihood given a relative change in the value of the indicated parameter. The vertical line indicates the relative default value of the parameter (Tables S1 and S3) and the red dot points at the value corresponding to the highest likelihood score. The horizontal bar delimits the 95% confidence interval overlaid with the corresponding absolute parameter value. The inset shows the full range of variation while the larger panel magnifies the area around the confidence interval (shaded in gray). (**A-D**) Optimized unmeasured parameters of the mutual inhibition terms. Note that the best value for α (**B**, red dot) was not reached because a simulation cannot be initialized with this value; instead a default initialization value was used in this analysis. (**E-L**)

Remaining parameters of the model. (**M-O**) Parameters of the temperature adaptation terms. Note that E_ν is perfectly symmetric because the absolute value of the activation energies are used. (**P-Q**) Dimension parameters of the cell. (**R**) Scaling factor for the cortical flows.

Supporting References

1. Abràmoff, M., P. Magalhães, and S. Ram. 2004. Image processing with ImageJ. Biophotonics Int. 11: 36–42.
2. Amer, A., and E. Dubois. 2005. Fast and reliable structure-oriented video noise estimation. IEEE Trans. Circuits Syst. Video Technol. 15: 113–118.
3. Blanchoud, S., Y. Budirahardja, F. Naef, and P. Gönczy. 2010. ASSET: a robust algorithm for the automated segmentation and standardization of early *Caenorhabditis elegans* embryos. Dev. Dyn. an Off. Publ. Am. Assoc. Anat. 239: 3285–96.
4. Goldstein, B., and S.N. Hird. 1996. Specification of the anteroposterior axis in *Caenorhabditis elegans*. Development. 122: 1467–74.
5. Rappleye, C. a, A. Tagawa, R. Lyczak, B. Bowerman, and R. V Aroian. 2002. The anaphase-promoting complex and separin are required for embryonic anterior-posterior axis formation. Dev. Cell. 2: 195–206.
6. Bellman, R. 1952. On the theory of dynamic programming. Proc. Natl. Acad. Sci. U. S. A. 38: 716–9.
7. Goehring, N.W., P.K. Trong, J.S. Bois, D. Chowdhury, E.M. Nicola, et al. 2011. Polarization of PAR proteins by advective triggering of a pattern-forming system. Science. 334: 1137–41.
8. 2010. NIST Handbook of mathematical functions. In: Olver FWJ, DW Lozier, RF Boisvert, CW Clark, editors. New York, NY: Cambridge University Press.
9. Goehring, N.W., C. Hoege, S.W. Grill, and A.A. Hyman. 2011. PAR proteins diffuse freely across the anterior-posterior boundary in polarized *C. elegans* embryos. J. Cell Biol. .
10. Hansen, N., and A. Ostermeier. 2001. Completely derandomized self-adaptation in evolution strategies. Evol. Comput. 9: 159–95.
11. Lagarias, J.C., J.A. Reeds, M.H. Wright, and P.E. Wright. 1998. Convergence properties of the Nelder--Mead simplex method in low dimensions. SIAM J. Optim. 9: 112–147.
12. Filzmoser, P., R. Maronna, and M. Werner. 2008. Outlier identification in high dimensions. Comput. Stat. Data Anal. 52: 1694–1711.
13. Munro, E., J. Nance, and J.R. Priess. 2004. Cortical flows powered by asymmetrical contraction transport PAR proteins to establish and maintain anterior-posterior polarity in the early *C. elegans* embryo. Dev. Cell. 7: 413–24.
14. Jaqaman, K., D. Loerke, M. Mettlen, H. Kuwata, S. Grinstein, et al. 2008. Robust single-particle tracking in live-cell time-lapse sequences. Nat. Methods. 5: 695–702.
15. Olivo-Marin, J.-C. 2002. Extraction of spots in biological images using multiscale products. Pattern Recognit. 35: 1989–1996.
16. Smith, C.S., N. Joseph, B. Rieger, and K. a Lidke. 2010. Fast, single-molecule localization that achieves theoretically minimum uncertainty. Nat. Methods. 7.
17. Niwayama, R., K. Shinohara, and A. Kimura. 2011. Hydrodynamic property of the cytoplasm is sufficient to mediate cytoplasmic streaming in the *Caenorhabditis elegans* embryo. Proc. Natl. Acad. Sci. U. S. A. 108: 11900–5.

18. Tseng, Q., E. Duchemin-Pelletier, A. Deshiere, M. Balland, H. Guillou, et al. 2012. Spatial organization of the extracellular matrix regulates cell-cell junction positioning. Proc. Natl. Acad. Sci. U. S. A. 109: 1506–11.
19. Kawai, M., T. Kido, M. Vogel, R.H. a Fink, and S. Ishiwata. 2006. Temperature change does not affect force between regulated actin filaments and heavy meromyosin in single-molecule experiments. J. Physiol. 574: 877–87.
20. Laidler, K.J. 1985. Chemical kinetics and the origins of physical chemistry. Arch. Hist. Exact Sci. 32: 43–75.
21. Dell, A.I., S. Pawar, and V.M. Savage. 2011. Systematic variation in the temperature dependence of physiological and ecological traits. Proc. Natl. Acad. Sci. U. S. A. 108: 10591–6.
22. Doremus, R.H. 2002. Viscosity of silica. J. Appl. Phys. 92: 7619.
23. Hird, S.N. 1996. Cortical actin movements during the first cell cycle of the *Caenorhabditis elegans* embryo. J. Cell Sci. 109: 525.
24. Cheeks, R.J., J.C. Canman, W.N. Gabriel, N. Meyer, S. Strome, et al. 2004. *C. elegans* PAR proteins function by mobilizing and stabilizing asymmetrically localized protein complexes. Curr. Biol. 14: 851–62.
25. Mayer, M., M. Depken, J.S. Bois, F. Jülicher, and S.W. Grill. 2010. Anisotropies in cortical tension reveal the physical basis of polarizing cortical flows. Nature. .
26. Bieler, J., C. Pozzorini, and F. Naef. 2011. Whole-embryo modeling of early segmentation in *Drosophila* identifies robust and fragile expression domains. Biophys. J. 101: 287–96.